Piezo-optical response of Ge in the visible–uv range

P. Etchegoin, J. Kircher, M. Cardona, and C. Grein*
Max-Planck-Institut für Festkörperforschung, Heisenbergstrasse 1, D-7000 Stuttgart 80, Germany
(Received 12 November 1991)

Using rotating-analyzer ellipsometry we have measured the three complex components $P_{11}(\omega)$, $P_{12}(\omega)$, and $P_{44}(\omega)$ of the linear piezo-optical tensor $P_{ijkl}(\omega)$ of Ge in the 1.6 – 5.6 eV photon energy range. This was accomplished by applying static uniaxial stress to Ge crystals along the [111] and [001] crystallographic directions, and monitoring the stress-induced changes in the dielectric function $\epsilon(\omega)$ at room temperature. The real and imaginary parts of each component were directly obtained. They show, in general, good Kramers-Kronig consistency. A comparison with pseudopotential calculations of $P_{11}(\omega)$, $P_{12}(\omega)$, and $P_{44}(\omega)$ for strained Ge is also given. In addition, deformation-potential constants ($D_1^1, D_1^5, D_3^3, D_3^5$) and spin-exchange parameters ($\delta_{J_1}, \delta_{J_2}$) were determined for the $E_1 - E_1 + \Delta_1$ transitions; they show good agreement with prior work.

I. INTRODUCTION

The effect of external modulations on the optical properties of semiconductors has been a subject of active research for a long time. It is possible to study effects due either to differential modulations such as cubic perturbations (like hydrostatic pressure or temperature changes) or to noncubic perturbations like uniaxial stresses or electric fields.[1] In particular, the effect of strains on the principal optical transitions in Ge has been studied before, using techniques such as piezo-electroreflectance,[2] stress-induced birefringence,[3] piezoreflectance,[4] and ac-strain modulation of the reflectivity.[5] The effect of strains on the optical response has also been studied theoretically using group theoretical methods.[6] However, a direct measurement of the real and imaginary parts of the components of the linear piezo-optical tensor using ellipsometric techniques is still not available. The principal advantage of such techniques, in contrast to reflectivity measurements, is that no additional assumptions (extrapolations at low and high energies required by the Kramers-Kronig analysis) are needed to obtain the real and the imaginary components of $\epsilon(\omega)$ [i.e., $\epsilon_1(\omega)$ and $\epsilon_2(\omega)$]. Another advantage is that stress-induced macroscopic deformations of the sample surface leave ellipsometric measurements largely undisturbed, since ellipsometry is a self-normalizing method with respect to either incident or reflected light intensity.

In this paper, we present ellipsometric measurements of the linear optical response functions of Ge under uniaxial stress. These measurements allowed us to obtain directly the experimental value of the complex components $P_{11}(\omega)$, $P_{12}(\omega)$, and $P_{44}(\omega)$ in the visible–uv range ($\sim$ 1.66 to $\sim$ 5.5 eV). To the best of our knowledge this work represents the first application of spectral ellipsometry to the determination of piezo-optic functions.

From the theoretical point of view, it is possible in principle to obtain the piezo-optical tensor by calculating the dielectric function of the strained crystal from its electronic structure using any standard band-structure calculation technique. We have performed such calculations with the empirical pseudopotential method (EPM) and found reasonable agreement with the experimental data.

In this paper, we first focus our discussion on the experimental results obtained, including the determination of the deformation-potential constants for the $E_1 - E_1 + \Delta E_1$ transitions (Sec. II). The theoretical predictions for the piezo-optic functions obtained from the pseudopotential band-structure calculations are reported and discussed in Sec. III.

We conclude this introduction by mentioning that the variation of the dielectric tensor of semiconductors with stress is receiving renewed interest in branches of semiconductor physics such as strained superlattices, Raman scattering by folded acoustic modes in such superlattices, and the design of optomechanical devices. On the other hand, ellipsometry is emerging as a powerful tool for *in situ* characterization of the growth process of semiconductor layers.[7] Our results should help in the interpretation of growing processes when the Ge overlayers are stressed due to lattice mismatch on different substrates.

II. EXPERIMENT

A. Experimental setup and samples

Rotating-analyzer ellipsometry (RAE) is a well-established technique to measure the complex dielectric function $\epsilon(\omega)$. Details about the technique are discussed in the literature.[8,9] Essentially, the ellipsometric measurements provide the frequency-dependent complex reflectance ratio between s- and p-polarized light. These values can be converted to $\epsilon(\omega)$ assuming a model for the reflection process. In particular we exploit the fact that for weakly anisotropic semi-infinite samples with a large dielectric function, the ellipsometric data provide

a good approximation to the projection of the dielectric tensor onto the intersection of the plane of incidence and the sample surface.[10] In the following we will emphasize only those general aspects of the apparatus and the experimental procedure of particular importance for the present work.

The optical path was kept in air and the angle of incidence was set to 67.5°. We used a Xe lamp as a light source and a 2400-lines/mm grating with the slits of the monochromator at 1 mm (monochromator length= 0.75 m). The polarizer azimuth was fixed to 30° with respect to the plane of incidence. The light reflected by the sample was modulated by means of a Rochon prism rotating at 2200 rpm. The signal was obtained using conventional photo-counting techniques as an average of 150 revolutions of the analyzer per duty cycle and 70 revolutions per dark cycle. Mirror optics was used to collimate and focus the light. The sample was optically aligned using a visible laser (He-Ne) with the monochromator set to zeroth-order reflection. All data were taken with a mesh between 10 and 20 meV. Conventional calibration procedures have been followed.[8] The complex reflectance ratio is automatically converted to $\epsilon(\omega)$ assuming the simplest model for the reflection process, that is, a sharp interface between an infinite medium and air. All measurements were done at room temperature. Technical details of the ellipsometer itself are given in Ref. 11. Measurement in air has the advantage for ellipsometry that no additional depolarizing effects due to optical windows are present, but the price to be paid is the presence of an oxide layer on the surface which may vary with time.

The uniaxial stress was applied with a hydraulic-stress machine developed especially for that purpose.[12] Our apparatus is not yet able to measure in vacuum and provides only compressive stress.

The bulk material used to fabricate the samples was commercial high-purity Ge with a resistivity of 40 Ω cm at room temperature. Crystals were cut with the longest side in the [111] and [001] directions and oriented using Laue x-ray diffraction. The sample surfaces were mechanically polished and treated immediately before the measurements with a wet chemical etching previously suggested.[13]

B. Data evaluation

The optical properties of strained cubic crystals are described, in general, by symmetric second-rank tensors $n_{ij}(\omega)$ and $k_{ij}(\omega)$ (optical constants), or $\epsilon_{1_{ij}}(\omega)$ and $\epsilon_{2_{ij}}(\omega)$. In the following we shall concentrate on the effect of a noncubic perturbation (uniaxial stress) on the optical properties of Ge. Measurements in which the symmetry of the crystal is lowered by the uniaxial stress are of particular interest; the properties involve a larger number of functions which can be discussed in terms of the lowered symmetry and the appropriate selection rules.

For a cubic crystal, the variation of $\epsilon_2(\omega)$ (to first order) induced by a stress along either of the principal directions [100] or [111] is given by

$$\Delta\epsilon_2(\omega) = \begin{pmatrix} \Delta\epsilon_2^{\perp}(\omega) & 0 & 0 \\ 0 & \Delta\epsilon_2^{\perp}(\omega) & 0 \\ 0 & 0 & \Delta\epsilon_2^{\parallel}(\omega) \end{pmatrix},$$

where the third axis is taken parallel to the strain axis. The corresponding change in $\epsilon_1(\omega)$ can be computed from $\Delta\epsilon_2(\omega)$ using Kramers-Kronig analysis. For small stresses the components $\Delta\epsilon_2(\omega)$ are assumed to be proportional to the applied force per unit area $\mathbf{X}$ (stress). For $\mathbf{X}$ along [001] or [111] the crystal becomes uniaxial; this is not true for stress along [110] or a lower symmetry direction. The case of a general stress direction is described by the piezo-optical tensor $P_{ijkl}(\omega)$ which connects the second-rank dielectric tensor $\epsilon_{ij}(\omega)$ to the second-rank stress tensor X_{kl}. The linear piezo-optical tensor $P_{ijkl}(\omega)$ satisfies $P_{ijkl} = P_{jikl} = P_{ijlk} = P_{mn}$, i.e., it can be specified in general by a symmetric matrix with indices $m, n = 1...6$ (i=j=1→m=1; i=1, j=2→m=6 and index permutations). Here we are only interested in the cubic case. For cubic crystals that belong to the classes 432, $\bar{4}3m$, and $m\bar{3}m$ the number of independent $P_{mn}(\omega)$'s can be reduced. Germanium is included in this case since its point group is $m\bar{3}m$ (O_h). Only three different $P_{mn}(\omega)$'s are needed in this case.[14] Different conventions have been used in the past for the piezo-optic coefficients, most of them relating $\Delta[\epsilon_{ij}^{-1}](\omega)$ with the strain tensor u_{kl} (or, alternatively, with the stress).[14] Since we are measuring the dielectric function itself using a direct method, we found it more convenient to use "piezo-optic coefficients" that relate the change in each component of the tensor, $\Delta\epsilon_{ij}(\omega)$, to the stress tensor. We thus use the definition

$$\Delta\epsilon_{ij}(\omega) = P_{ijkl}(\omega)X_{kl} \tag{1}$$

because it is the natural choice for our experiment and the primary output of the theoretical calculations. In our measurements the stress ($\mathbf{X}$) [Pa] has been applied in the [111] and [001] directions. For each direction, and each stress, we performed two measurements to find the component of $\epsilon(\omega)$ in the direction parallel and perpendicular to the stress. For the crystal stressed along [111], measurements of $\epsilon(\omega)$ were performed on the (211) face, while for the stress along [001], they were taken on the (100) face. From a first measurement we obtained $\epsilon^{\parallel}(\omega)$ and from a second one $\epsilon^{\perp}(\omega)$, for each stress direction. By calculating the difference of each spectrum under stress with the unstressed spectrum $\epsilon(\omega)$ we obtained $\Delta\epsilon^{\parallel}(\omega)$ and $\Delta\epsilon^{\perp}(\omega)$. The information that can be obtained from each experiment is given in a compact form in Eq. (1). The predictions of this equation for our experimental geometries are summarized in Table I. We have used the convention that $\mathbf{X}$ is negative when the sample is compressed.

In principle only three independent measurements are needed to obtain all the components of the piezo-optical tensor. We have measured four configurations, only three of which are therefore independent. The additional set of results can be used to check the consistency of the data since it must lead to a linear combination of the three independent components of $P_{ij}(\omega)$.

TABLE I. Proportionality between $\Delta\epsilon(\omega)$ and X for different crystallographic directions and polarizations.

X	Face	E	$\Delta\epsilon(\omega)$
		Longitudinal	
[001]	(100)	[001]	$P_{11}X$
[111]	(211)	[111]	$\frac{1}{3}(P_{11}+2P_{12}+P_{44})X$
		Transverse	
[001]	(100)	[010]	$P_{12}X$
[111]	(211)	[011]	$\frac{1}{3}(P_{11}+2P_{12}-1/2P_{44})X$

After $\epsilon(\omega)$ has been obtained for all configurations and several stresses, we fit the variation of $\epsilon(\omega)$, for fixed ω, as a function of the stress to a straight line. From the slope of this fit we obtain the corresponding piezo-optical tensor component. The dependence of $\epsilon(\omega)$ on $\mathbf{X}$ is usually linear up to $|\mathbf{X}| \sim 500$–700 MPa except very close to interband critical points. The samples break in general when $|\mathbf{X}| \sim 1000$ MPa.

Since the sample was kept in air during the measurements, the presence of an oxide layer on its surface was unavoidable. After etching the crystal[13] and mounting it in the stress apparatus we had a residual oxide layer of about 10 Å for the [001] and ~20 Å for the [211] faces. In order to find the exact oxide thickness for the unstressed samples we fitted our data using a three-phase model (substrate/oxide/air) in which the bulk values for $\epsilon(\omega)$ from Ref. 13, and the dielectric function for amorphous GeO_2 tabulated by Devyatykh *et al.*,[15] were used as fixed values. This procedure, which has been widely used in the literature,[13] was performed in a region ~1 eV around 4.2 eV (E_2 transitions) since the penetration depth of light is near its minimum there and thus the ellipsometric parameters are most sensitive to surface layers. The assumption of an amorphous GeO_2 layer on top of a mechanically polished surface turns out to be good for the evaluation of optical data. The thickness of the oxide layer at the end of a complete series of measurements (10 to 15 spectra taken at different stresses in ascending order, taking about 30 h in total) was in the range between 25 and 35 Å. This was detected by taking another $\mathbf{X}=\mathbf{0}$ spectrum at the end of the series and again employing the above-described procedure.

We assumed a growing law for the oxide layer $d(t)$ as a function of time of the form

$$d(t) = d_f + (d_0 - d_f)\exp(-\alpha t) , \tag{2}$$

where d_0 is the thickness of the oxide layer at $t = 0$, d_f the corresponding saturation value, and α a constant to be fitted. We interpolated the different values for the layer in the strained samples using a fit for d_0, d_f, and α. The fit was performed with the values for $d(t)$ obtained from the three-phase model in three to four unstressed spectra taken at different stages of the experiment. The agreement between the experimental $d(t)$ and the value predicted by Eq. (2) after the fitting was always better than 20%. Every stressed spectrum was numerically corrected after the experiment using the fitted thickness $d(t)$. This means fitting the data with a three-phase model (see above) but leaving the thickness and optical constants of the oxide film fixed, and varying $\epsilon(\omega)$ of the substrate. With this method we obtained $\epsilon(\omega)$ for the bare surface at different stresses. The important assumption here is that the dielectric properties of the oxide layer are not modified when the stress is being applied. This is a reasonable assumption, at least for GeO_2 (Ref. 15), which is an insulator with critical points far from the visible region. Its dielectric function has only a real component and is also smooth and flat in the experimental region of interest. Also, we believe that the applied stress to the bulk of the crystal is not felt as much on the oxidized surface. Possible effects due to the surface layer are further minimized by obtaining the piezo-optical functions from the slope of $\epsilon(\omega)$ vs stress for fixed ω. We checked that different assumptions for the oxide layer did not much influence the final result.

In general a noticeable effect of the stress on the critical-point transitions is expected due to the symmetry breaking of the crystal point group. Consistency with the Kramers-Kronig relation should hold for the so obtained components of the piezo-optical tensor since they are derivatives of the linear susceptibilities with respect to the applied stress.

Several optical functions, such as the reflectivity, are related to $\epsilon_1(\omega)$ and $\epsilon_2(\omega)$. We have calculated some of them in order to compare our data with previous works in this area, in particular ac-modulated strain reflectance and piezoreflectance. We do not discuss piezo-optical measurements performed with techniques such as electroreflectance,[2] since they involve a more complicated modulation process which makes difficult a direct comparison of the measurements. The measured differential reflectivity as a function of the strain can be compared with our data, taking into account that a change in the dielectric function $\epsilon(\omega)$ induces a change in the reflectivity given by

$$\frac{\Delta(R^{\parallel,\perp}(\omega))}{R(\omega)} = \alpha\Delta\{\mathrm{Re}[\epsilon^{\parallel,\perp}(\omega)]\} + \beta\Delta\{\mathrm{Im}[\epsilon^{\parallel,\perp}(\omega)]\} , \tag{3}$$

where α and β are the Seraphin coefficients[16] and $\parallel$ and $\perp$ refer to the direction of the component of the dielectric tensor with respect to $\mathbf{X}$.

However, deformation-potential constants derived from piezo-optical data can be compared easily with results of electroreflectance.[2,17] The evaluation of those constants for the critical point transitions $E_1 - E_1 + \Delta_1$ is given in the following subsection.

C. Evaluation of deformation-potential constants for the $E_1 - E_1 + \Delta_1$ critical points

Ellipsometry yields directly the dielectric function of the investigated sample with very high numerical precision and is therefore the most appropriate technique to investigate the characteristics of optically allowed inter-

band critical points. The nature of the $E_1 - E_1 + \Delta_1$ transitions in Ge has been discussed for the first time by Phillips.[18] The corresponding structure in optical spectra is now known to arise from transitions in the Λ direction of the Brillouin zone (BZ) {111}. The dimensionality of the transitions has also been extensively discussed in the literature.[19–24] Here we use the model of Ref. 19: each of the transitions E_1 and $E_1 + \Delta_1$ is produced by a mixture of a 2D minimum and a saddle point which can be expressed by

$$\epsilon(\omega) \sim C - \ln(E - \hbar\omega - i\Gamma)\exp(i\phi) , \tag{4}$$

where E is the critical-point energy (threshold or gap), Γ the broadening, and ϕ takes into account the amount of mixture ($0 \leq \phi \leq \pi/2$).[23,25,26] If no exciton effects are present at the critical point, and if the chosen dimensionality is correct, ϕ is restricted to one of the values $\phi = 0, \pi/2, \pi$ for 2D critical points, and represents a geometrical characteristic of the electronic bands in the $\mathbf{k}$ space at that energy. For E_1 and $E_1 + \Delta_1$ ϕ would be zero, corresponding to an interband minimum. Exciton effects can be included phenomenologically using intermediate values of ϕ.[26] Our fits gave $\phi \sim 60°$ at room temperature for the unstressed samples, in good agreement with previous results.[19,27] Since E_1 and $E_1 + \Delta_1$ are very close, it is necessary to fit both critical points at the same time. In fact, the second derivatives of $\epsilon(\omega)$ (real and imaginary parts) are fitted instead of $\epsilon(\omega)$ itself. This is done to enhance the spectral structure related to the critical points. The 2D fits of the second derivatives for each component of $\epsilon(\omega)$ were thus performed with the functions [using Eq. (4)]

$$\left\{\frac{d^2\epsilon(\omega)^{\parallel,\perp}}{d\omega^2}\right\}_{E_1} = -\frac{I^{\parallel,\perp}_{E_1} e^{i\phi}}{(E - \hbar\omega - i\Gamma)^2} , \tag{5}$$

$$\left\{\frac{d^2\epsilon(\omega)^{\parallel,\perp}}{d\omega^2}\right\}_{E_1+\Delta_1} = -\frac{I^{\parallel,\perp}_{E_1+\Delta_1} e^{i\phi}}{(E + \Delta_1 - \hbar\omega - i\Gamma)^2} , \tag{6}$$

where $I^{\parallel,\perp}_{E_1}$ and $I^{\parallel,\perp}_{E_1+\Delta_1}$ are the so-called strengths (or amplitudes) of each critical point and $\parallel$ and $\perp$ refer to the appropriate component of $\epsilon(\omega)$ with respect to $\mathbf{X}$. The phase ϕ has been forced to be the same for both transitions during the fits.[19] From the simultaneous fits of the real and imaginary parts of the second derivatives in the range 1.8 eV $\leq \hbar\omega \leq$2.7 eV we obtained the energy thresholds for both transitions E_1 and $E_1 + \Delta_1$ as a function of the stress ($\mathbf{X}$) for both components of $\epsilon(\omega)$ ($\parallel$ and $\perp$).

The effect of $\mathbf{X}$ on the critical-point energy can result in (i) shifts due to the hydrostatic component of the strain, (ii) intraband splittings of degenerate states, and (iii) interband splittings of the various equivalent $\mathbf{k}$'s if $\mathbf{k} = \mathbf{k}_e = \mathbf{k}_h \neq 0$ (see Ref. 2 for details). The shifts and splittings of critical-point energies for a particular direction of $\mathbf{X}$ can be described by appropriate deformation-potential constants. The deformation-potential concept is rather old; it was introduced by Bardeen and Shockley[28] in 1950.

Using the appropriate excitonic basis, it has been shown[29,30] that the effective Hamiltonian (including spin-exchange interactions) for $E_1 - E_1 + \Delta_1$ has the following eigenvalues (for $\mathbf{X}\|[001]$):

$$\begin{aligned} E_1(\mathbf{X}) = {} & E_1(0) + (3)^{-1/2} D_1^1 (S_{11} + 2S_{12})\mathbf{X} \\ & - (\tfrac{2}{3}) \frac{(D_3^3)^2 (S_{11} - S_{12})^2}{\Delta_1} \mathbf{X}^2 \\ & \pm 2\delta_{J_1} (\tfrac{2}{3})^{1/2} \frac{(D_3^3)(S_{11} - S_{12})}{\Delta_1} \mathbf{X} \end{aligned} \tag{7}$$

and

$$\begin{aligned} E_1 + \Delta_1(\mathbf{X}) = {} & (E_1 + \Delta_1)(0) + (3)^{-1/2} D_1^1 (S_{11} + 2S_{12})\mathbf{X} \\ & + (\tfrac{2}{3}) \frac{(D_3^3)^2 (S_{11} - S_{12})^2}{\Delta_1} \mathbf{X}^2 \\ & \pm 2\delta_{J_2} (\tfrac{2}{3})^{1/2} \frac{(D_3^3)(S_{11} - S_{12})}{\Delta_1} \mathbf{X} , \end{aligned} \tag{8}$$

where D_1^1 is the deformation potential for hydrostatic strain, D_3^3 represents the intraband effect of a [001] shear on the top valence bands, and δ_{J_1}, and δ_{J_2} are the spin-exchange terms. S_{ij} are elastic-compliance constants. The expansions of (7) and (8) hold when $\Delta_1 \gg$intraband term$\gg$spin-exchange term.

The difference observed between the critical energies of E_1 and $E_1 + \Delta_1$ for polarizations parallel and perpendicular to $\mathbf{X}\|[001]$ cannot be understood on the basis of one-electron theory. However, by including the spin exchange for the electron-hole interaction this difference can in principle be explained. Experimentally it is observed that the spin-exchange terms are somewhat different for E_1 and $E_1 + \Delta_1$. Such a difference can only be explained by assuming additional mixing with other states not included in our description. These spin-exchange terms are in general very small and difficult to measure.

For $\mathbf{X}\|[111]$ the stress introduces a preferential direction [111] (singlet) and leaves the other three valleys $[\bar{1}\,\bar{1}1]$, $[\bar{1}1\,\bar{1}]$, and $[1\bar{1}\,\bar{1}]$ as equivalent (triplet). The effective Hamiltonian for the singlet has no off-diagonal interband elements and its eigenvalues (neglecting the contribution of exchange interactions) are[29,30]

$$\begin{aligned} E_1^S(\mathbf{X}) = {} & E_1(0) - (3)^{-1/2} D_1^1 (S_{11} + 2S_{12})\mathbf{X} \\ & + (12)^{-1/2} D_1^5 S_{44} \mathbf{X} \end{aligned} \tag{9}$$

$$\begin{aligned} (E_1 + \Delta_1)^S(\mathbf{X}) = {} & (E_1 + \Delta_1)(0) \\ & - (3)^{-1/2} D_1^1 (S_{11} + 2S_{12})\mathbf{X} \\ & + (12)^{-1/2} D_1^5 S_{44} \mathbf{X} \end{aligned} \tag{10}$$

where the deformation potential D_5^1 represents the intervalley effect of a [111] shear strain.

Using again the appropriate excitonic basis and expanding in powers of $(\Delta(\mathbf{X})/\Delta_1)$, the eigenvalues for the triplet become

$$E_1^T(\mathbf{X}) = E_1(0) - (3)^{-1/2}D_1^1(S_{11}+2S_{12})\mathbf{X} - (12)^{-1/2}D_5^1 S_{44}\mathbf{X} - (\tfrac{2}{27})\left(\frac{(D_3^5)^2}{\Delta_1}\right)S_{44}^2\mathbf{X}^2+\cdots \quad (11)$$

and

$$(E_1+\Delta_1)^T(\mathbf{X}) = (E_1+\Delta_1)(0) - (3)^{-1/2}D_1^1(S_{11}+2S_{12})\mathbf{X} - (12)^{-1/2}D_5^1 S_{44}\mathbf{X} + (\tfrac{2}{27})\left(\frac{(D_3^5)^2}{\Delta_1}\right)S_{44}^2\mathbf{X}^2+\cdots . \quad (12)$$

D_3^5 is the deformation potential that describes the intravalley effect in the valence bands. It produces nonlinearities in the dependence of the triplet energy on stress which are equal and opposite for E_1 and $E_1+\Delta_1$. Symmetry considerations indicate that the triplet is seen for both components of the dielectric tensor ($\|$ and $\perp$) when $\mathbf{X}\|[111]$. On the other hand, the singlet is seen only for the perpendicular component.[2] Exchange terms due to the coupling of the electron and the hole in the exciton basis can also be included in the Hamiltonian, but their effect seems to be small in this case since it is not observed experimentally.

We fitted the energy position of the critical points, as obtained from the best fit of the second derivatives of $\epsilon(\omega)$, to a line or a parabola in order to obtain the relevant deformation-potential constants. The principal assumptions made for the evaluation of the deformation potentials were (i) the excitonic contribution described by ϕ is the same for both transitions and (ii) Δ_1 is not a function of $\mathbf{X}$. We took the value of Δ_1=0.202 eV obtained at room temperature[19] as fixed.

Since we are fitting the real and the imaginary parts of $\epsilon(\omega)$ in a region of the order of 1 eV around the critical-point transitions, our method is potentially more accurate with respect to previous ones, for example, the three-point method used to evaluate the Schottky-barrier electroreflectance.[17]

D. Results

We first show in Fig.1 the real and imaginary parts of the dielectric function obtained for the unstressed case. They have been corrected for the contribution of the oxide layer as explained in Sec. II B. These results are the starting point for our experiments. In Fig. 1 we include the experimental values from Table III of Ref. 13, obtained with a very clean surface at room temperature. The height of $\epsilon_2(\omega)$ at the E_2 transitions ($\hbar\omega \sim 4.2$ eV) is the same since we forced the values to agree with those of Ref. 13 in our fitting procedure (see Sec. II B). However some small differences exist near the $E_1-E_1+\Delta_1$ transitions [relative heights of E_1 and $E_1+\Delta_1$ in $\epsilon_1(\omega)$]. These small differences, which cannot be compensated with the assumption of a homogeneous overlayer with known $\epsilon(\omega)$, are sometimes associated with roughness at the surface

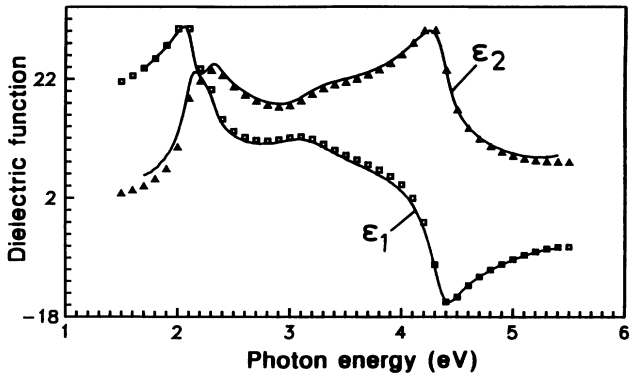

FIG. 1. Real and imaginary parts of $\epsilon(\omega)$ for $\mathbf{X}=0$ after corrections for the GeO_2 layer. Solid symbols are data from Ref. 13 which we are using as a reference spectrum to obtain the oxide layer on the surface.

related to differences in the polishing procedure. We anticipate their effect to be small for our purposes.

Figure 2 shows, in an expanded scale, the behavior of $\epsilon_2^{\|}(\omega)$ for three different stresses $|\mathbf{X}|$=0, 217, and 435 MPa along [001]. From linear fits of $\epsilon_1(\omega)$ and $\epsilon_2(\omega)$ vs $|\mathbf{X}|$, (see inset in Fig. 2) at fixed photon energies we extracted the main results of this paper which are shown in Fig. 3. $P_{11}(\omega)$ has been obtained from $\epsilon(\omega)$ parallel to the stress along [001], i.e., $\Delta\epsilon_{[001]}^{\|}(\omega)$, and $P_{12}(\omega)$ from $\Delta\epsilon_{[001]}^{\perp}(\omega)$ (see Table I). $P_{44}(\omega)$ is extracted from the difference between the parallel and the perpendicular components of the dielectric tensor for $\mathbf{X}$ along [111], i.e.,

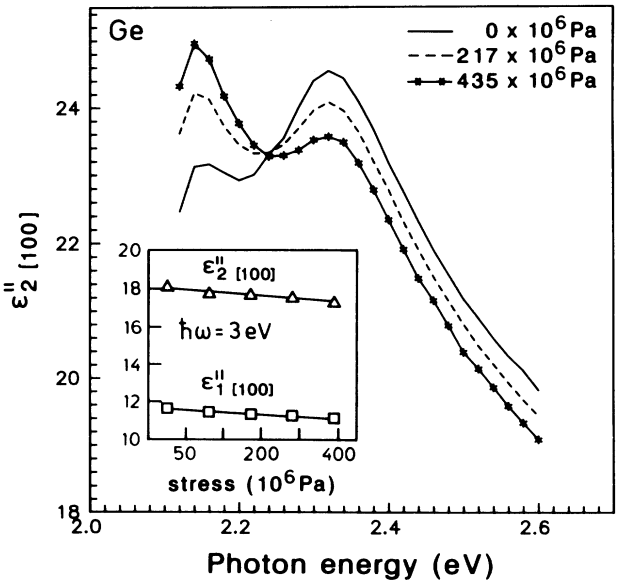

FIG. 2. $\epsilon_2^{\|}(\omega)$ for three different stresses. $\mathbf{X}$ was applied along [001] (or equivalent directions). The inset shows $\epsilon_1(\omega)$ and $\epsilon_2(\omega)$ vs $\mathbf{X}$ for a fixed photon energy ($\hbar\omega$=3 eV) within the linear variation range.

$$P_{44}(\omega) = 2\frac{[\Delta\epsilon^{\parallel}_{[111]}(\omega) - \Delta\epsilon^{\perp}_{[111]}(\omega)]}{\Delta X} . \quad (13)$$

As mentioned before, it is possible to use one of the four measurements for a self-consistency check of the piezo-optical functions. For example, we may obtain $P_{44}(\omega)$ using $\Delta\epsilon^{\parallel}_{[111]}$ and subtracting the appropriate contribution of $P_{11}(\omega)$ and $P_{12}(\omega)$ found in the measurements with **X** along [001] (see Table I). It is also possible to check such a consistency by calculating the hydrostatic contribution for both crystallographic directions $[(\Delta\epsilon^{\parallel} + 2\Delta\epsilon^{\perp})/2]$ (Γ_1 component). We checked the self-consistency in both ways and found it to be good.

The piezo-optic functions $P_{ij}(\omega)$, as derivatives of $\epsilon(\omega)$'s, are constrained by Kramers-Kronig dispersion relations between their real and imaginary parts. In the case of $\epsilon(\omega)$ it is often difficult to obtain fully satisfactory Kramers-Kronig consistency checks because of the restricted experimental frequency range and the need to extrapolate the data to infinite and zero frequencies. For differential quantities, such as the $P_{ij}(\omega)$'s, with strong structure at critical points, the influence of the extrapolations is less important. We performed such a verification using $\mathrm{Im}(P_{ij})$ to calculate $\mathrm{Re}(P_{ij})$, using

$$\mathrm{Re}[P_{ij}(\omega)] = (-2/\pi)P\int \frac{\Omega\,\mathrm{Im}[P_{ij}(\Omega)]}{(\Omega^2 - \omega^2)}d\Omega + C , \quad (14)$$

where C is a constant and P means the principal value of the integral. We did not include in the numerical evaluations of Eq. (14) data above 5.6 eV and below 1.66 eV, and assumed that most of their effect is taken care of by the *ad hoc* constant C. It is therefore expected that the result of such numerical evaluations will differ somewhat from the measured ones at both ends of the spectra. Results showing a satisfactory comparison between experimental and calculated $\mathrm{Re}[P_{ij}(\omega)]$ using Eq. (14) are given in Fig. 4 for each component of the tensor. The close agreement provides additional confidence to our experimental results.

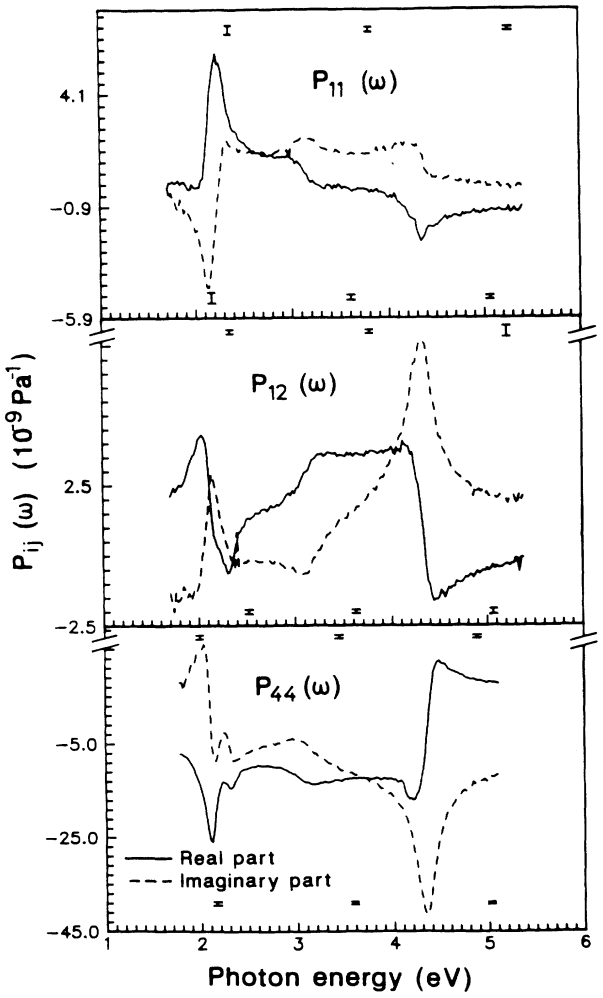

FIG. 3. Real and imaginary parts of the three independent piezo-optical components of Ge. The error bars that are shown on top of each curve correspond to $\mathrm{Re}[P_{ij}(\omega)]$ at the corresponding energy. The error bars at the bottom are for the imaginary part.

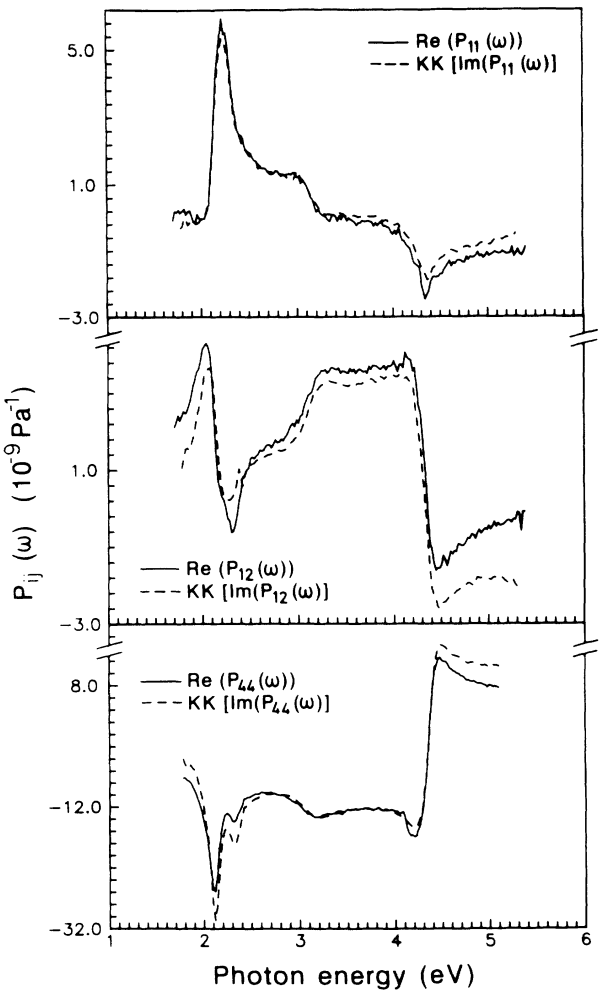

FIG. 4. Consistency checks for the experimental and Kramers-Kronig-computed [with Eq.(14)] real parts of the components of the piezo-optical tensor $P_{ij}(\omega)$.

From the complex $\epsilon(\omega)$ measured for different stresses we calculated related optical properties to compare them with previous results. For both samples we evaluated the reflectivity for each component of the dielectric tensor (parallel $\parallel$ and perpendicular $\perp$ to **X**) ; the results are plotted in Fig. 5. The reflectivity for each case was calculated using the values for $\epsilon(\omega)$ corrected for the presence of an oxide layer. We also calculated $(1/R)dR/d\mathbf{X}$ numerically for **X** along [111] using $\epsilon^{\parallel}_{[111]}(\omega)$ and obtained the result displayed in Fig. 6. In order to compare them we summarize some previous results in Fig. 7. Our real and imaginary parts of $P_{44}(\omega)$ (Fig. 3) can be compared with the result obtained by Kramers-Kronig analysis of piezoreflectance data.[22] Results of such evaluations near $E_1 - E_1 + \Delta_1$ are included in Fig. 7(a). In contrast to our data for the piezo-optical constants, those given in Fig.7(a) are in arbitrary units as is expected from piezoreflectance. Previous determinations of the stress dependence of the polarized reflectivity in the region near $E_1 - E_1 + \Delta_1$ (Ref. 4) are included in Fig. 7(b) as well as $\Delta R(\omega)/R(\omega)$ (Ref. 5) for one particular direction in Fig. 7(c), as seen with ac-strain-modulated reflectivity. Figure 7(b) can be compared favorably with the calculated reflectivity components shown in Fig. 5 for **X**$\parallel$[001], even if the strains are not exactly the same. The result of Fig.7(c) should be proportional to the calculated $(1/R)dR/d\mathbf{X}$ shown in Fig.6. The same structures are observed at the critical points, as expected. The offset between both results is artificial; it is due to the fact that the absolute zero is arbitrary in Fig. 7(c) (Ref. 5). The sign reversal between the curves of Figs. 6 and 7(c) is irrelevant.

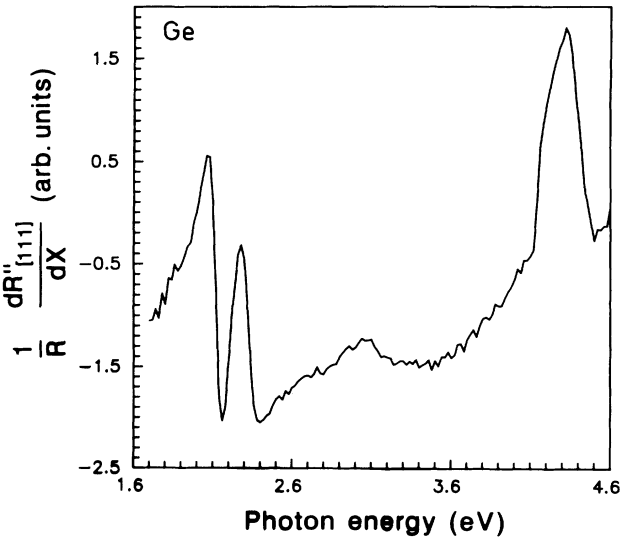

FIG. 6. Calculated derivative of the reflectivity with respect to **X** along [111], using Eq.(3) and the parallel component of $\epsilon(\omega)$ in that configuration. The features are similar to those obtained with ac-modulated strain reflectivity.

In Fig. 8 we show the hydrostatic component of the

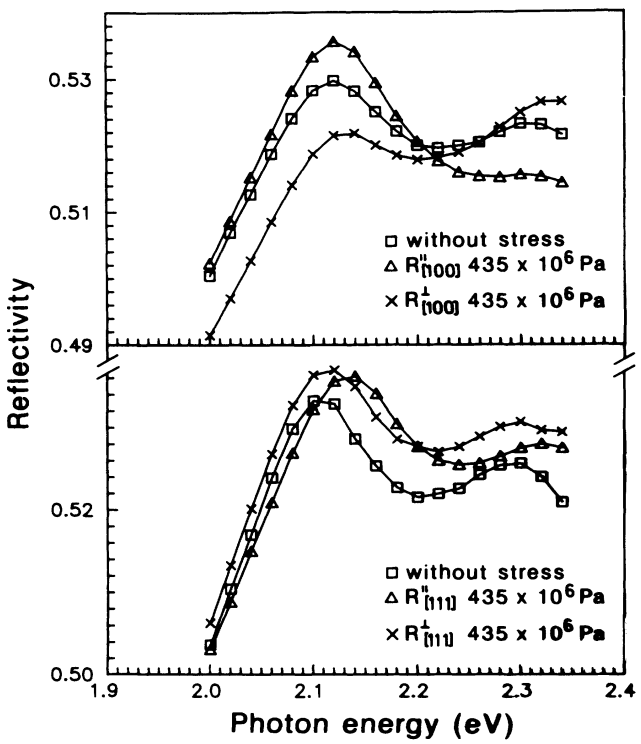

FIG. 5. Calculated reflectivity for both [111] and [001] stresses using the $\epsilon(\omega)$ components in the direction $\parallel$ and $\perp$ to **X**=435 MPa in each case.

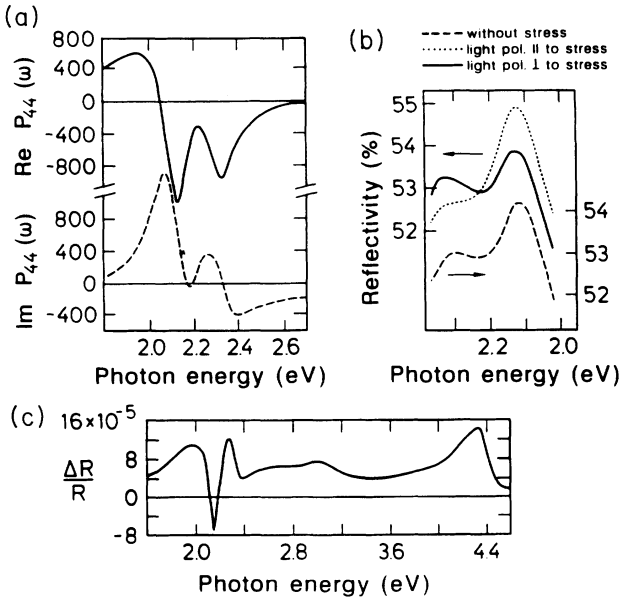

FIG. 7. (a) Real and imaginary parts of $P_{44}(\omega)$ obtained by piezoreflectance and the use of the Kramers-Kronig relations (Ref. 22). (b) Dependence of the reflectivity as a function of the polarization ($\parallel$,or $\perp$ to **X**) near $E_1 - E_1 + \Delta_1$ from Ref. 4. Results correspond to **X**$\parallel$[001]. The unstressed reflectivity is in a different scale (right). The stressed results for the $\parallel$ and $\perp$ polarizations with respect to **X** are obtained with a fixed strain component along the stress axis (0.4%) (compression). (c) ac-strain modulation of the reflectivity from Ref. 5.

tensor $[P_{11}(\omega) + 2P_{12}(\omega)]$, and also $[P_{11}(\omega) - P_{12}(\omega)]$, i.e., the irreducible symmetry components of $P_{ij}(\omega)$ for **X** along [001] (Γ_1 and Γ_{12} components).[6]

The critical-point analysis to obtain the deformation-potential constants of the $E_1 - E_1 + \Delta_1$ critical points was performed as follows.

1. **X**||[001] . We define $\overline{E_1}$ and $\overline{E_1 + \Delta_1}$ by averaging the two eigenvalues of Eqs. (7) and (8), to eliminate the contribution of δ_{J_1} and δ_{J_2}. Likewise, the sum $\frac{1}{2}(\overline{E_1} + \overline{E_1 + \Delta_1})$ is independent of the nonlinear intravalley terms $\propto (D_3^3)^2$. This sum can be fitted to a line to obtain D_1^1. The values of $\frac{1}{2}(\overline{E_1} + \overline{E_1 + \Delta_1})$ as a function of the stress are displayed in Fig. 9. The value of D_1^1 found in this manner is given in Table II. Those of $\overline{E_1}$ and $\overline{E_1 + \Delta_1}$ can be used to obtain D_3^3 by fitting their dependence on **X** with a parabola. These fits are also shown in Fig. 9. The values for D_3^3 obtained from both curves are given in Table II. Following Chandrasekhar and Pollak,[17] δ_{J_1} and δ_{J_2} were calculated using results for E_1 and $E_1 + \Delta_1$ for one direction (|| or $\perp$) with the value of D_3^3 obtained above. The agreement with the room temperature data of Ref. 17 is quite good (see Table II).

The strengths of the transitions for both critical points have also been calculated using perturbation theory. With the notation of Ref. 2 we have

$$I^{\parallel}_{E_1}(\mathbf{X}) = I^{\parallel}_{E_1}(0)(1 + \alpha_1) , \tag{15}$$

$$I^{\parallel}_{E_1+\Delta_1}(\mathbf{X}) = I^{\parallel}_{E_1+\Delta_1}(0)(1 - \alpha_1) , \tag{16}$$

$$I^{\perp}_{E_1}(\mathbf{X}) = I^{\perp}_{E_1}(0)(1 - 1/2\alpha_1) , \tag{17}$$

$$I^{\perp}_{E_1+\Delta_1}(\mathbf{X}) = I^{\perp}_{E_1+\Delta_1}(0)(1 + 1/2\alpha_1) , \tag{18}$$

where $\alpha_1 = \delta E_{100}/\Delta_1$ and $\delta E_{100} = \sqrt{8/3} D_3^3 (S_{11} - S_{12})\mathbf{X}$. These are linear expansions in α_1. In Fig. 10 we show the values obtained for the ratio of strengths $[(I^{\parallel}/I^{\perp})_{E_1, E_1+\Delta_1}]$ as a function of stress. The solid curve represents the predictions of Eqs. (15) to (18) with the value of D_3^3 obtained above. The agreement with the measured stress dependences of the strength ratios is remarkably good.

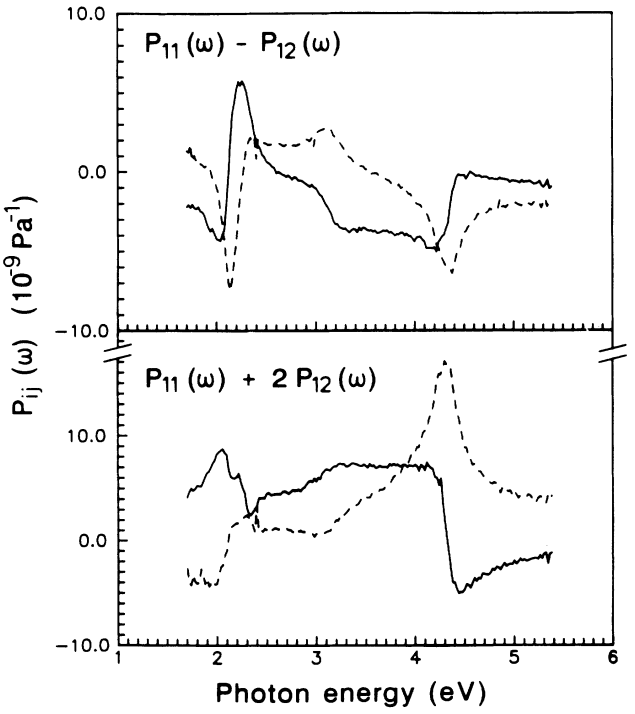

FIG. 8. Irreducible components of $P_{ij}(\omega)$ for **X**||[001]. $[P_{11}(\omega) + 2P_{12}(\omega)]$ transforms as Γ_1 (hydrostatic component) under the symmetry operations of the crystal. $[P_{11}(\omega) - P_{12}(\omega)]$ corresponds to the Γ_{12} irreducible representation.

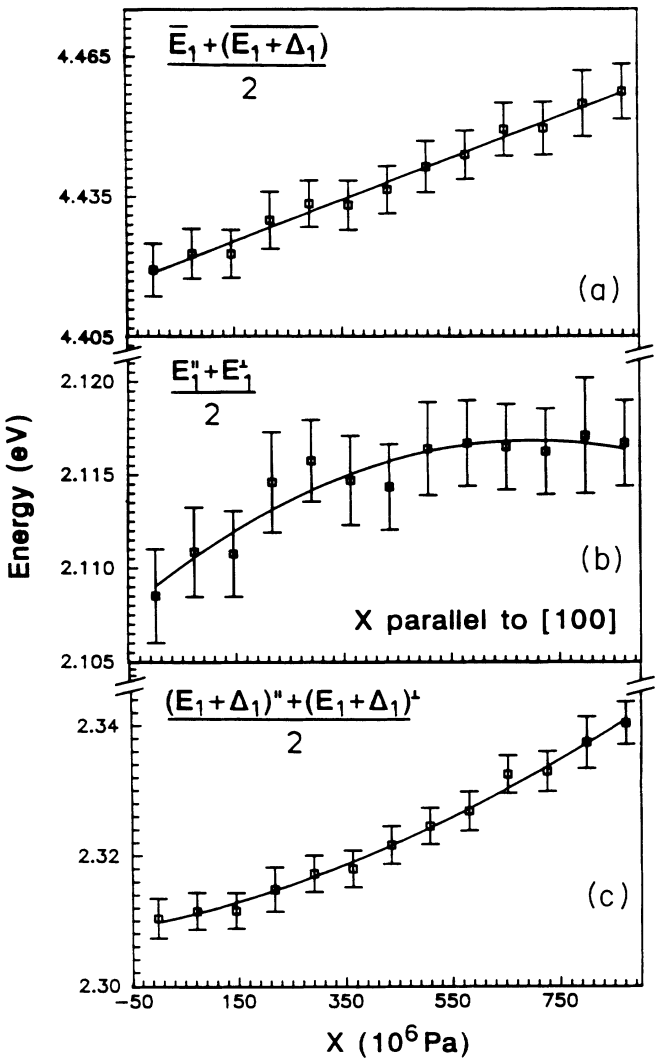

FIG. 9. (a) $\frac{1}{2}[\overline{E_1} + \overline{E_1 + \Delta_1}(\mathbf{X})]$ vs **X**. The slope is proportional to D_1^1 and the obtained value is shown in Table II. (b) and (c) correspond to $\overline{E_1}$ and $\overline{E_1 + \Delta_1}$ and can be used to obtain D_3^3 by fitting both with a parabola. The solid curves are the best fits in each case.

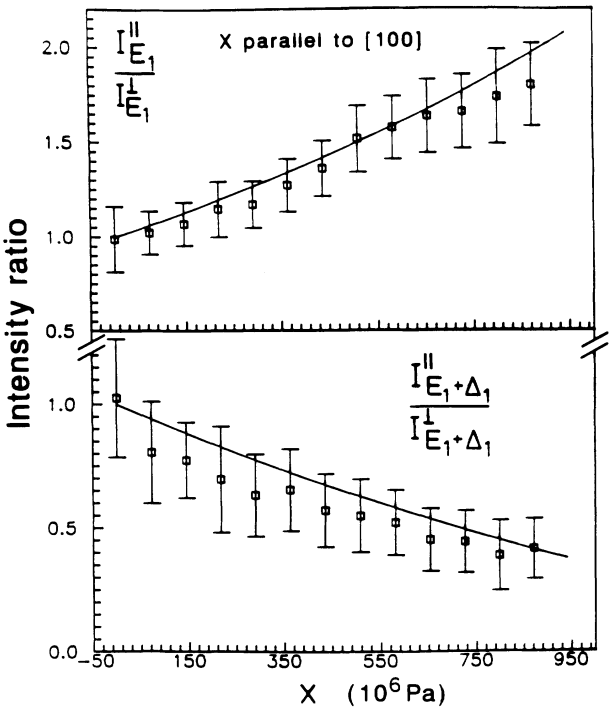

FIG. 10. Intensity ratios for each of the critical points E_1 and $E_1+\Delta_1$ as a function of X||[001]. The solid curves represent the theoretical predictions obtained with Eqs.(15) to (18) and the value of D_3^3 evaluated from the shift of the energy thresholds for both CP's.

Conversely, the stress dependence of these ratios allows us to obtain the sign of D_3^3 which cannot be ascertained from the fits of the critical points energies since it depends only on the square of D_3^3. Figure 10 shows that D_3^3 is negative. It should be kept in mind that **X** is actually negative (compression), meaning that a positive slope in the figures corresponds to a negative D_3^3.

2. X||[111]. In this case we analyze the component of $\epsilon(\omega)$ parallel to **X** (triplet only), for which the deformation-potential constants D_1^1, D_1^5, and D_3^5 are important. From Eqs. (11) and (12) it is clear that the values for $\frac{1}{2}[E_1^T+(E_1+\Delta_1)^T]$ are independent of the intravalley term proportional to D_3^5. They can be fitted to a straight line to obtain D_1^5 using the value for D_1^1 that had been previously found (X||[001]). The result is shown in Fig. 11(a). The D_1^5 so obtained is displayed in Table II.

The dependence of E_1^T on **X** for X||[111] is shown in Fig.11(b) with the solid line representing the best linear fit. The curvature introduced by the quadratic effect of the intravalley term is very small. This is in agreement with previous results;[2] D_3^5 is masked by the linear portion and the experimental uncertainties. In view of the large experimental errors it is not possible to extract a meaningful value of D_3^5 from E_1^T. We obtained D_3^5 from the dependence of the peak strengths on **X**. The strengths for **X** along [111] and for all possible configurations are also reported in Ref. 2. The linear expansions of the intensities with respect to **X** are given by

$$I^{\parallel}_{E_1}(\mathbf{X}) = I^{\parallel}_{E_1}(0)(1+4/3\alpha_2)\ , \tag{19}$$

$$I^{\parallel}_{E_1+\Delta_1}(\mathbf{X}) = I^{\parallel}_{E_1+\Delta_1}(0)(1-4/3\alpha_2)\ , \tag{20}$$

$$I^{\perp}_{E_1}(\mathbf{X}) = I^{\perp}_{E_1}(0)(1-4/3\alpha_2)\ , \tag{21}$$

$$I^{\perp}_{E_1+\Delta_1}(\mathbf{X}) = I^{\perp}_{E_1+\Delta_1}(0)(1+4/3\alpha_2)\ , \tag{22}$$

where $\alpha_2=\delta E_{111}/\Delta_1$ and $\delta E_{111}=\sqrt{1/6}D_3^5(S_{44})\mathbf{X}$.

In Fig. 11(c) we also show the experimental ratios

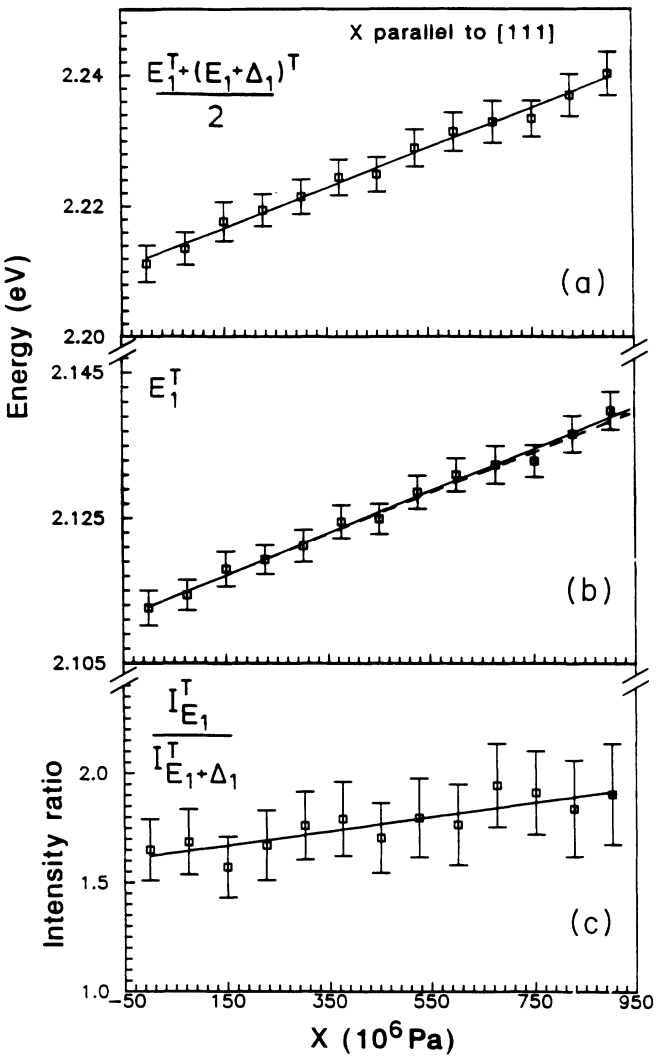

FIG. 11. Energy thresholds and intensity dependence for the triplet for X||[111]. In (a) we show the stress dependence of $\frac{1}{2}[E_1^T+(E_1+\Delta_1)^T]$. (b) and (c) display E_1^T and the intensity ratio $I^{\parallel}_{E_1}/I^{\parallel}_{E_1+\Delta_1}$. From the latter we obtained $D_3^5=-3.1\pm0.9$ using a linear fit. E_1^T is plotted with the best linear fit (solid line) and the theoretical prediction [Eq. (11)] (dashed line) using the obtained D_3^5 (see text for details).

$(I^{\parallel}_{E_1}/I^{\parallel}_{E_1+\Delta_1})$ as a function of $\mathbf{X}\|[111]$. The theoretical prediction is given by the ratio of Eq. (19) to Eq. (20). Since α_2 is small, we can assume a linear behavior for this ratio and fit the experimental data to a straight line. The best fit is shown in the same figure. From the slope of this fit we obtained $D_3^5 = -3.1 \pm 0.9$. This value is reinserted in Eq. (11) and plotted together with E_1^T in Fig. 11(b) (dashed line). The agreement is good within the experimental error. In this case we have analyzed only the stress dependence for the ratios of parallel intensities because the perpendicular components, mixtures of singlet and triplet, are not subject to simple analysis. However, the strength ratio $(I_{E_1}/I_{E_1+\Delta_1})$ at $\mathbf{X}=0$ can be compared with theoretical predictions. Within the framework of the microscopic one-electron model of Ref. 35 the strength ratio at $\mathbf{X}=0$ is given by

$$I_{E_1}(0)/I_{E_1+\Delta_1}(0) \simeq \frac{(E_1+\Delta_1/3)(E_1+\Delta_1)^2}{(E_1)^2(E_1+2\Delta_1/3)} . \qquad (23)$$

This model predicts a strength ratio ~1.12, which underestimates the experimental result. This theoretical estimate can be improved by adding the "linear terms in $k^{\perp}_{[111]}$" as discussed in Ref. 36. The main effect of those terms is to increase the transverse mass for the E_1 gap and decrease that for $E_1+\Delta_1$. The corrected strength ratio in this case is ~1.64, which compares remarkably well with our experimental determination at $\mathbf{X}=0$ (see Fig. 11).

The obtained value for D_3^5 obtained from $(I^{\parallel}_{E_1}/I^{\parallel}_{E_1+\Delta_1})$ is in agreement with some previous results[22,37] but disagrees with the value reported in Refs. 17 and 31. We believe that our result is more accurate than the earlier ones; we shall return to this matter in the discussion of results.

With respect to the phase (ϕ), which gives the excitonic character of the critical point, we found that for the best quality data used in the numerical analysis of the derivatives of $\epsilon(\omega)$, the phase remains constant in the range $50° - 60°$. This suggests that the excitonic character of the critical points E_1 and $E_1+\Delta_1$ is not changed significantly by the stress. The binding energy for such excitations can be modified if the effective dielectric function changes drastically or if the effective mass is strongly affected. The stress-induced changes in $\epsilon(\omega)$ are too small to affect the binding energy seriously. The strain-induced changes in the effective mass can also be estimated to be small.

E. Analysis of errors

In general, when the light intensity is strong enough, ellipsometric data are well outside the regime in which statistical errors are important. It is possible to obtain smooth spectra and smooth derivatives up to second and third order. However, since we are interested in small stress-induced differences in the data, special care must

TABLE II. Deformation-potential constants and spin-exchange parameters for the $E_1 - E_1+\Delta_1$ transitions, compared to other measurements.

D_1^1 (eV)	D_1^5 (eV)	D_3^3 (eV)	D_3^5 (eV)	δ_{J_1} (meV)	δ_{J_2} (meV)	Ref.
$-9.6 \pm 0.8^{a,b}$	$11.3 \pm 1.1^{a,b}$	$5.8 \pm 0.6^{b,c}$	$6.1 \pm 1.5^{a,b}$	$0 \pm 0.5^{b,c,h}$		
$-8.2 \pm 0.7^{c,b}$		$5.9 \pm 0.6^{c,f}$		$4.3 \pm 0.4^{c,f,g}$	$2 \pm 0.2^{c,f,h}$	17
$-8.1 \pm 0.8^{c,d}$	5.9 ± 1.2^{d}					
$-9.9 \pm 0.5^{d,e}$						4
-9.7 ± 1^{f}	7.5 ± 0.8^{f}	$2.2^{+1}_{-0.5}$ ^{f}	$1.5^{+0.6}_{-0.3}$ ^{f}			37
-7.8 ± 0.7	8.5 ± 0.8	2.6 (at k = 0)	6.4 (at k = 0)			2
-8.1 ± 0.8^{f}		5.9 ± 0.6^{f}		4.3 ± 0.4^{f}	2.0 ± 0.2^{f}	29
		3.0 ± 0.3	5.7 ± 0.6			31
-8.6	6.0					32
-9.5 ± 0.5						33
-10.7						34
-10.4 ± 0.5	8.5 ± 0.6	3.4 ± 0.3	2.4 ± 0.3			
-9.2 ± 0.5		3.6 ± 0.4	2.5 ± 0.4			22
$-8.6 \pm 0.5^{c,f,g,h}$	$-12.2 \pm 0.5^{a,f,g,h}$	$-5.6^{+0.6}_{-0.2}$ ^{c,f,g}	$-3.1 \pm 0.9^{a,f,i}$	$6.5 \pm 0.7^{c,f}$	$2.9 \pm 0.3^{c,f}$	
		$-6.2^{+0.4}_{-0.1}$ ^{c,f,h}				present work

[a] $X \parallel [111]$.

[b] 77 K.

[c] $X \parallel [001]$.

[d] U. Gerhardt in Ref. 4 and also in Phys. Status Solidi **11**, 801 (1965).

[e] R. Zallen and W. Paul, Phys. Rev. **155**, 703 (1967).

[f] 300 K.

[g] E_1 peak.

[h] $E_1 + \Delta_1$ peak.

[i] $I^{\parallel}_{E_1}/I^{\parallel}_{E_1+\Delta_1}$ for $\mathbf{X}\|[111]$.

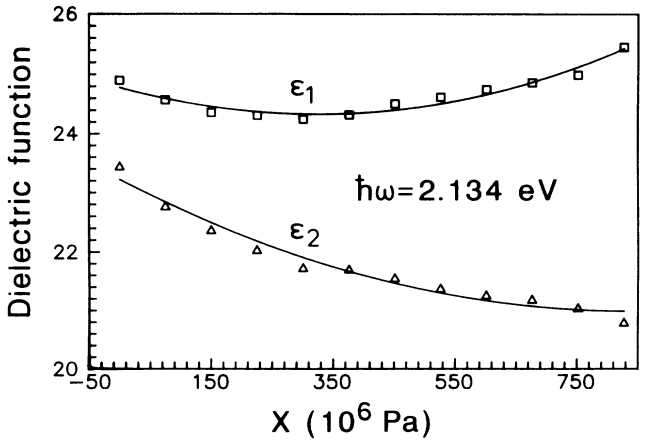

FIG. 12. Nonlinearities for both $\epsilon_1(\omega)$ and $\epsilon_2(\omega)$ as a function of $|\mathbf{X}|$ at fixed photon energy. The nonlinear region has been discarded for the evaluation of the $P_{ij}(\omega)$ components.

be taken. We tested the signal at fixed ω to check the statistical errors during a long period of time. It turned out that for our setup the absolute statistical errors were of the order of 10^{-2} in $\epsilon(\omega)$ at frequencies below~2 eV, and of the order of 10^{-3} above. In calculating the errors we assumed a constant statistical error of 10^{-2} for the full spectral range for both the real and the imaginary parts of $\epsilon(\omega)$.

The applied force was measured with an accuracy of 0.5% and our stress apparatus showed a creeping of only ~3 N after a given stress. The sample area was measured to within 0.02 mm^2. This means a relative error for the stress, assuming it to be homogeneous, of the order of 20% at 40 Pa (the lowest stress applied) and better than 2% for higher stresses. The resolution of our monochromator with the slits at 1.5 mm varies in the range 1–10 meV for our experimental range.

The error bars that are shown in the figures for the piezo-optical components were calculated assuming that the stress is exactly known and including both the statistical error for $\epsilon(\omega)$ and the error in the slope of the linear fit.

As we mentioned before, we sometimes reached the region in which the variation of $\epsilon(\omega)$ with stress is no longer linear. In those cases the behavior of $\epsilon(\omega)$ above a certain stress has been discarded for the fit to obtain the components of $P_{ij}(\omega)$. A typical nonlinear behavior of $\epsilon(\omega)$ at fixed photon energy is shown in Fig. 12. The number of points used for the fit of the components of $P_{ij}(\omega)$ was different from one sample to another and for different photon energies, but in any case we used at least five different stress points (for fixed energy) showing a good linear behavior to obtain the $P_{ij}(\omega)$'s. A typical linear fit is shown in the inset of Fig. 2. The nonlinearities of $\epsilon(\omega)$ are useful for the critical-point analysis and we used in that case the full stress range until the sample broke ($\mathbf{X}$~1000 MPa) to analyze the $E_1 - E_1 + \Delta_1$ transitions.

The error bars shown in the fits for the critical-point parameters are obtained by numerical means and represent only the error of the fit. Our program uses a χ^2 test to obtain the error in each case and the fitted parameters are given with 95 – 98% confidence. The errors for the deformation-potential constants were calculated using the error for the fit and the error bar for each point. In the case of D_3^3 the nonlinearity of the curve introduces a nonsymmetric error bar for these constants. This is not the case for D_3^5 because we obtained its value from the fit of the intensity dependence (see above) which is linear in D_3^5. The data showed good reproducibility for different samples. The measurements were repeated for a total of four [001] and six [111] samples with the same surface treatment.

III. PSEUDOPOTENTIAL CALCULATIONS

The application of the pseudopotential method to the calculation of optical properties of semiconductors has been extensively discussed.[38] Our calculations were performed without spin-orbit coupling. A few details of the procedure are given below.

For an unstressed lattice it suffices to perform band structure calculations in the reduced first Brillouin zone (i.e., $\frac{1}{48}$th of the full BZ for diamondlike structures). However, when the symmetry is broken due to the presence of stress, a lower point group obtains and sampling of more points is needed. We use the full BZ taking 2361 points to avoid miscellaneous numerical problems at the expense of redundant CPU time.

When the lattice is strained, lattice points in real space change from $\mathbf{r}$ to $\mathbf{r}^* = \mathbf{r} + \Delta(\mathbf{r})$, inducing a change in the reciprocal space vectors from $\mathbf{k}$ to $\mathbf{k}^* = \mathbf{k} - \Delta(\mathbf{k})$. The values of the Fourier components of the pseudopotential for the strained lattice were linearly interpolated between the nearest well-known values for the unstrained lattice[38,39] (for $\mathbf{G} = \sqrt{3}, \sqrt{8}, \sqrt{11}$). In this way, we have obtained the pseudopotential that allowed us to calculate

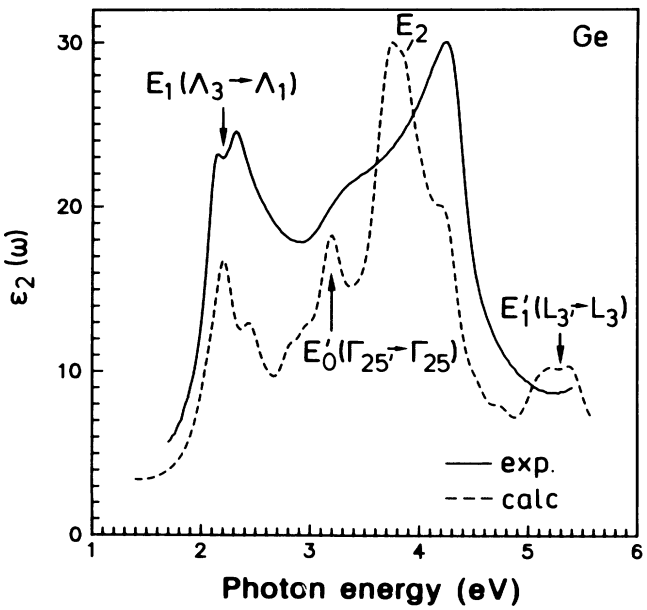

FIG. 13. Experimental and calculated $\epsilon_2(\omega)$ for unstrained Ge using EPM. Some typical critical points in the visible–uv region are explicitly shown.

the band structure and the optical response under stress. The deformation in real space was calculated, for a given force, using the room-temperature elastic constants.[40] The new position for each lattice point in real space when **X** is present is calculated to first order in the deformation tensor $\overleftrightarrow{\varepsilon}$. This means that if $\mathbf{r}^* = (\overleftrightarrow{1} + \overleftrightarrow{\varepsilon}) \cdot \mathbf{r}$, the corresponding change of a reciprocal lattice vector is given by $\mathbf{k}^* = (\overleftrightarrow{1} - \overleftrightarrow{\varepsilon}) \cdot \mathbf{k}$. To determine the relative sublattice deformations under [111] stress we also used the appropriate internal stress parameter ($\zeta = 0.577$) obtained from a fit of the phonon dispersion relation with a planar force model with electronic degrees of freedom.[41] The lattice parameters were taken to be those at room temperature. The band structure was computed with the interpolated pseudopotential. This makes it possible to calculate $\epsilon_2(\omega)$ by taking into account all direct transitions at a given energy among the calculated bands using

$$\epsilon_2(\omega) = \frac{4\pi^2 e^2 \hbar}{3m^2\omega^2} \times \sum_{c,v} \frac{2}{(2\pi)^3} \int_{\mathrm{BZ}} |\langle u_{i,\mathbf{k}} | \nabla | u_{j,\mathbf{k}} \rangle|^2 \times \delta(E_c(\mathbf{k}) - E_v(\mathbf{k}) - \omega) d\mathbf{k} \,. \quad (24)$$

To evaluate Eq. (24) we used for $\delta(E)$ a Lorentzian with a small broadening Γ_0. We performed the summation with different broadenings and used the one that showed best agreement with the experimental value of $\epsilon_2(\omega)$ at E_2 [$\epsilon_2(\hbar\omega$=4.2 eV)$\sim$30].

In the computation of $\epsilon_2(\omega)$ the contribution of the first four valence bands below the gap and 14 conduction bands above it was included. In general, the higher conduction bands are poorly represented by the empirical pseudopotential method. Our cutoff for the summation is just where the energy denominators make the contribution to $\epsilon(\omega)$ very small.

Theoretical results

The $\epsilon_2(\omega)$ calculated for the unstrained lattice using pseudopotentials is compared with the experiment in Fig. 13. Similar pseudopotential results can be seen in Ref. 42. The additional peak at $\hbar\omega \sim$2.4 eV in the calculation is not due to spin-orbit coupling since the latter has not been taken into account. This feature has been observed before in band-structure calculations without spin-orbit coupling performed with the $\mathbf{k} \cdot \mathbf{p}$ method,[43,44]

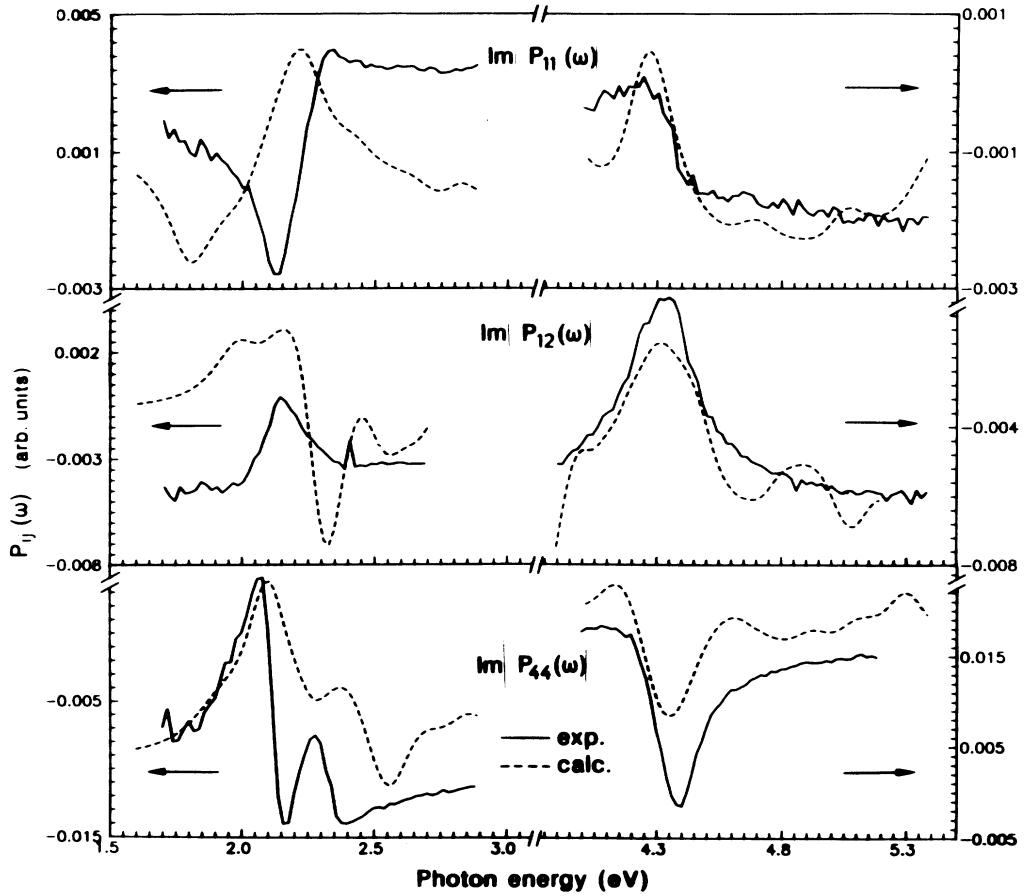

FIG. 14. Experimental and calculated (using EPM) imaginary parts of $P_{11}(\omega)$, $P_{12}(\omega)$, and $P_{44}(\omega)$ (see text for details). Only the energy range near the critical-point transitions E_1, $E_1 + \Delta_1$ and E_2 is shown. The theoretical calculation corresponds to |**X**|$\sim$2000 MPa. The units are arbitrary but the same for each pair of theoretical and experimental curves (compare with Fig.3).

and thus must be due to some peculiarity of the orbital bands. In order to obtain the piezo-optical components $P_{ij}(\omega)$ we found that it was not possible, for numerical reasons, to use in the calculation the small values of **X** used in the experiment. In fact, for the computation of $P_{ij}(\omega)$ we took **X**=2000 MPa. It is not obvious that results calculated in this manner will agree with the expansion for small $\overleftrightarrow{\varepsilon}$ under consideration although the lack of spin-orbit coupling may eliminate some of the source of nonlinearities. We computed only the imaginary part of the dielectric function and thus we will compare only imaginary parts of the $P_{ij}(\omega)$'s with theory. The various calculated components of $P_{ij}(\omega)$ are compared with the measured ones in Fig. 14. In order to display all results for different critical points and different components at the same time, the plots are given in arbitrary units (but the same for each pair of theoretical and experimental curves) and vertically shifted in some cases. Absolute units can be obtained by comparison of the experimental curves with those of Fig. 3. The agreement between theory and experiment is good, especially in view of the approximations involved, in particular the lack of spin-orbit coupling in the theoretical bands.

IV. DISCUSSION

The experimental results were shown to be (1) self-consistent with respect to measurements in different crystals ([111] and [001]), (2) Kramers-Kronig consistent, and (3) consistent with data for the polarized piezoreflectance and ac-strain-modulated reflectivity. This means that the ellipsometric data from which we are calculating the piezo-optical tensor are essentially correct. The contributions for $E_1 - E_1 + \Delta_1$ are in qualitative agreement with what one should expect for the intervalley and intravalley transitions in Ge (Ref. 2) (see Fig. 5).

Deformation-potential constants for the $E_1 - E_1 + \Delta_1$ transitions show good agreement with prior work except for D_3^5. We believe that a value of D_3^5 between -3 and -4 eV as obtained in our measurements should be essentially correct. Calculations of this constant using the pseudopotential method have been reported in Ref. 45. We reproduce in Fig. 15 the calculated D_1^5 (valence and conduction bands) and D_3^5 for Ge stressed along the [111] direction. The internal stress parameter for such calculation was taken to be $\zeta = 0.55$, a bit smaller than the one of Ref. 41. An average of D_3^5 on going from Γ to L within the first BZ gives a value of $|D_3^5| \sim 3.5-4$. The value obtained in Ref. 17 does not agree with such a calculation, while ours does. In Table III we include some theoretical values for the deformation-potential constants in order to compare them with our experimental results.

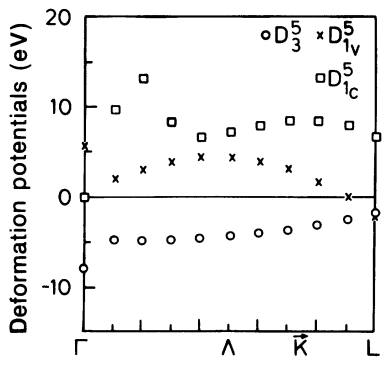

FIG. 15. Calculated deformation-potential constants D_3^5, $D_{1_v}^5$, and $D_{1_c}^5$ for Ge (at room temperature) using pseudopotentials from Ref. 45. Note that the absolute value and corresponding sign for D_3^5 agree well with our experimental determination.

TABLE III. Experimental and calculated deformation-potential constants for the $E_1 - E_1 + \Delta_1$ transitions.

	Present work (exp.)	Theory	Ref.
D_1^1	-8.6 ± 0.5	-6.9	46
		-8.6	32
		-8.1	47
D_1^5	-12.2 ± 0.5	3.9	46
		4.5	46
		6.0	32
D_3^3	$-5.6^{+0.6}_{-0.2}$	5.6[a]	48
D_3^5	-3.1 ± 0.9	-4[b]	45

[a] Absolute value obtained with LMTO.
[b] Average from Γ to L in the first BZ.

From a theoretical point of view we conclude that it is possible to obtain the essential features for $P_{ij}(\omega)$ using pseudopotential calculations. The fact that we had to use an unrealistically large strain in comparison with the experimental one in order to reproduce $P_{ij}(\omega)$ is probably related to the low density of **k** points used. No attempt has been made to explain the additional peak calculated near E_1 ($\hbar\omega \sim 2.4$ eV) since it should be strongly affected by spin-orbit coupling in a more realistic calculation. Some of the calculated peaks in $\mathrm{Im}(P_{ij})$ near E_1 are shifted with respect to the measurements. These shifts are to be expected since the spin-orbit coupling affects E_1 and we are not including it in the calculation. The agreement between theory and experiments near E_2 is significantly better.

We should also mention that we performed a critical-point analysis of the E_2 transitions. We found that good fits can be achieved assuming a single 2D critical point which is a mixture of a saddle point and a maximum ($\pi/2 \leq \phi \leq \pi$) in agreement with previous work.[19] We found that the average of the energy thresholds between the perpendicular and twice the parallel components for **X**||[001] gives a hydrostatic shift corresponding to $D_1^1(E_2) \sim -5.2 \pm 0.9$ eV, which is also in agreement with prior determinations.[22,34] However the shift for the || component is much larger than that of the $\perp$ one, thus indicating a shear effect. Since the detailed origin of E_2 is less clear[32,42,49–53] a complete analysis of this effect and its implications has not been performed and will be the subject of further analysis.

V. CONCLUSIONS

We have measured the piezo-optical response of Ge at room temperature using rotating-analyzer ellipsometry. From these measurements we obtained the components of the piezo-optical tensor $P_{11}(\omega)$, $P_{12}(\omega)$, and $P_{44}(\omega)$ between ~ 1.7 and ~ 5.4 eV. We also performed pseudopotential band-structure calculations (without spin-orbit coupling) of these tensor components and compared them with our measurements. The comparison at the critical points $E_1 - E_1 + \Delta_1$ and E_2 is satisfactory for all the components of the linear piezo-optical tensor. A complete *ab initio* band-structure calculation to compare directly with our results is still not available, but would be desirable. In addition, deformation-potential constants were determined for the $E_1 - E_1 + \Delta_1$ transitions, showing in general good agreement with prior measurements using different techniques.

A study of the piezo-optical response in the same photon energy range for GaAs and Si is in progress and will be published elsewhere.[54]

ACKNOWLEDGMENTS

Useful discussions with Dr. M. Garriga are gratefully acknowledged. Thanks are also due to H. Hirt, M. Siemers, and P. Wurster for expert technical help and to Dr. M. Kelly for his careful reading of a draft version of this paper. One of the authors (P.E.) would like to thank the Max-Planck-Gesellschaft for financial support.

*Present address: Division of Applied Sciences, Pierce Hall, Harvard University, Cambridge, MA 02138.

[1] Examples of stress modulation spectroscopy and related topics can be found in G. W. Gobeli and E. O Kane, Phys. Rev. Lett. **15**, 142 (1965); F. K. Pollak, Surf. Sci. **37**, 863 (1973); D. D. Sell and E. O. Kane, Phys. Rev. B **5**, 417 (1972); J. Koo, Y. R. Shen, and R. R. Zucca, Solid State Commun. **9**, 2229 (1971). A review of different related modulations is also given in Ref. 38.

[2] F. H. Pollak and M. Cardona, Phys. Rev. **172**, 816 (1968).

[3] M. Chandrasekhar, M. H. Grimsditch, and M. Cardona, Phys. Rev. B **18**, 4301 (1978).

[4] U. Gerhardt, Phys. Rev. Lett. **15**, 401 (1965).

[5] G. W. Gobeli and E. O. Kane, Phys. Rev. Lett. **15**, 142 (1965).

[6] E. O. Kane, Phys. Rev. **178**, 1368 (1969), and references therein.

[7] See, for example, D. E. Aspnes, W. E. Quinn, and S. Gregory, Appl. Phys. Lett. **57**, 2707 (1990).

[8] D. E. Aspnes and A. A. Studna, Rev. Sci. Instrum. **49**, 292 (1978).

[9] R. M. A. Azzam and N. M. Bashara, *Ellipsometry and Polarized Light* (North-Holland, Amsterdam, 1977).

[10] D. E. Aspnes, J. Opt. Soc. Am. **70**, 1275 (1980).

[11] M. Garriga, Ph.D. thesis, University of Stuttgart (1990).

[12] J. Kircher *et al.* (unpublished).

[13] D. E. Aspnes and A. A. Studna, Phys. Rev. B **2**, 985 (1983).

[14] For more details about these tensors see L. A. Shuvalov, in *Modern Crystallography IV (Physical Properties of Crystals)*, edited by H. J. Queĳsser, Springer Series in Solid-State Science Vol. 37 (Springer-Verlag, Berlin, 1988); I. Balslev, in *Semiconductors and Semimetals*, edited by R. K. Willardson and A. C. Beer (Academic, New York, 1972), Vol. 9.

[15] Devyatykh *et al.*, Kvant. Elektron. (Moscow) **7**, 1563 (1980) [Sov. J. Quant. Electron. **10**, 900 (1980)].

[16] B. Seraphin *et al.* , Phys. Rev. **145**, 628 (1966).

[17] M. Chandrasekhar and F. Pollak, Phys. Rev. B **15**, 2127 (1977).

[18] J. C. Phillips, J. Phys. Chem. Solids **12**, 208 (1960).

[19] L. Viña, S. Logothetidis, and M. Cardona, Phys. Rev. B **30**, 1979 (1984).

[20] S. Koeppen, P. Handler, and S. Jasperson, Phys. Rev. Lett. **27**, 265 (1971).

[21] J. Humlíček, Phys. Status Solidi B **86**, 303 (1978).

[22] J. Musilová, Phys. Status Solidi B **101**, 85 (1980).

[23] M. Cardona, in *Modulation Spectroscopy*, edited by F. Seitz, D. Turnbull, and H. Ehrenreich (Academic, New York, 1966).

[24] D. E. Aspnes and J. E. Rowe, Phys. Rev. B **7**, 887 (1973).

[25] J. E. Rowe and D. E. Aspnes, Phys. Rev. Lett. **25**, 162 (1970).

[26] D. E. Aspnes, in *Handbook on Semiconductors*, edited by T. S. Moss and M. Balkanski (North-Holland, Amsterdam, 1980).

[27] D. E. Aspnes, Phys. Rev. Lett. **28**, 168 (1972); D. E. Aspnes, in *Proceedings of the 12th International Conference on the Physics of Semiconductors, Stuttgart, 1974*, edited by M. H. Pilkhun (B. G. Teubner, Stuttgurt, 1974), Ref. 66, p. 1197; D. E. Aspnes and A. A. Studna, Surf. Sci. **96**, 294 (1980).

[28] J. Bardeen and W. Shockley, Phys. Rev. **80**, 72 (1950).

[29] M. Chandrapal and F. Pollak, Solid State Commun. **18**, 1263 (1976).

[30] J. E. Rowe, F. H. Pollak, and M. Cardona, Phys. Rev. Lett. **22**, 933 (1969).

[31] I. Balslev, Solid State Commun. **5**, 315 (1967).

[32] R. L. Saravia and D. Brust, Phys. Rev. **178**, 1240 (1969).

[33] E. Schmidt and K. Vedam, Solid State Commun. **9**, 1187 (1971).

[34] Y. F. Tsay, S. S. Mitra, and B. Bendow, Phys. Rev. B **10**, 1476 (1974).

[35] M. Cardona, in *Light Scattering in Solids II*, edited by M. Cardona and G. Güntherodt (Springer-Verlag, New York, 1982), p. 119.

[36] M. Cardona, Phys. Rev. B **15**, 5999 (1977).

[37] D. D. Sell and E. O. Kane, Phys. Rev. **185**, 1103 (1969).

[38] M. L. Cohen and J. R. Chelikowsky, in *Electronic Structure and Optical Properties of Semiconductors*, edited by M. Cardona, Springer Series in Solid-State Science Vol. 75 (Springer-Verlag, Berlin, 1988).

[39] M. L. Cohen and V. Heine, in *Solid State Physics*, edited by H. Ehrenreich, F. Seitz, and D. Turnbull (Academic, New York, 1970), Vol. 24.

[40] R.F.S. Hearmon, in *Elastic, Piezoelectric and Related Constants of Crystals*, edited by K.H. Hellwege and A. M. Hellwege Landolt-Börnstein, New Series, Group III, Vol. 11, (Springer-Verlag, Berlin, 1969), p. 27.

[41] P. Molinàs-Mata and M. Cardona, Phys. Rev. B **43**, 9799 (1991).

[42] D. Brust, J. C. Phillips, and G. F. Bassani, Phys. Rev. Lett. **9**, 94 (1962).

[43] C. W. Higginbotham, Ph.D. thesis, Brown University, 1967.
[44] C. W. Higginbotham, F. H. Pollak, and M. Cardona, Solid State Commun. **5**, 513 (1967).
[45] H. Presting, Ph. D. thesis, University of Stuttgart, 1985.
[46] P. J. Melz (unpublished).
[47] F. Herman, R. Kortum, C. D. Kuglin, and R. A. Short, in *Quantum Theory of Solids: A Tribute to J. C. Slater*, edited by Per-Olov Lowdin (Academic, New York, 1966), p. 381.
[48] U. Schmid, N. E. Christensen, and M. Cardona, Solid State Commun. **75**, 39 (1990).
[49] D. Brust, Phys. Rev. **134**, A1337 (1964).
[50] F. Bassani and D. Brust, Phys. Rev. **131**, 1524 (1963).
[51] G. Dresselhaus and M. S. Dresselhaus, Phys. Rev. **160**, 649 (1967).
[52] W. D. Grobman, D. E. Eastman, and J. L. Freeouf, Phys. Rev. B **12**, 4405 (1975).
[53] J. R. Chelikowsky and M. L. Cohen, Phys. Rev. Lett. **31**, 1582 (1973).
[54] P. G. Etchegoin, J. Kircher, M. Cardona, and C. Grein (unpublished).